ACS APPLIED MATERIALS & INTERFACES

Research Article

www.acsami.org

Effect of Pores in Hollow Carbon Nanofibers on Their Negative Electrode Properties for a Lithium Rechargeable Battery

Byoung-Sun Lee,[†] Seoung-Bum Son,[†,‡] Kyu-Min Park,[†] Geunsung Lee,[†] Kyu Hwan Oh,[†] Se-Hee Lee,[‡,§] and Woong-Ryeol Yu*[,†]

[†]Department of Materials Science and Engineering and Research Institute of Advanced Materials, Seoul National University, 599 Gwanangno, Gwanak-gu, Seoul 151-742, Republic of Korea

[‡]Department of Mechanical Engineering, University of Colorado, 427 UCB, Boulder, Colorado 80309, United States

[§]World Class University Hybrid Materials Program, Department of Materials Science and Engineering, Seoul National University, 599 Gwanangno, Gwanak-gu, Seoul 151-742, Republic of Korea

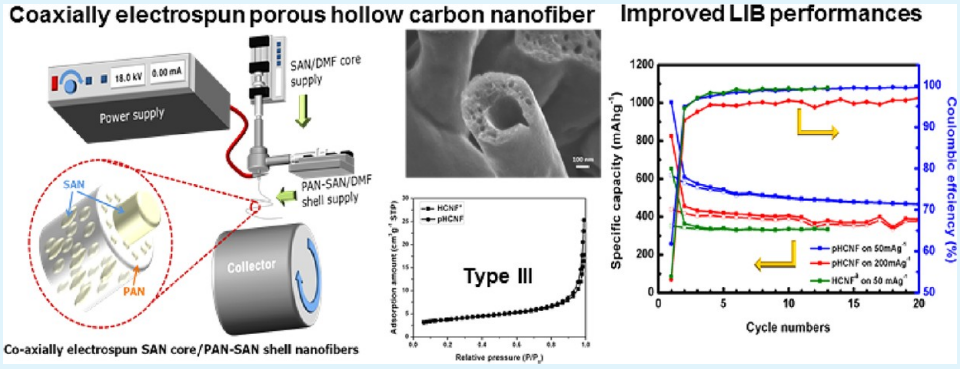

ABSTRACT: The effect of pores in hollow carbon nanofibers (HCNFs) on their electrochemical performance is investigated because the carbon shell itself acts as a reservoir for accommodating Li-ions through intercalation and simultaneously becomes a transport medium through which Li-ions migrate into the core materials in HCNFs. Porous HCNFs (pHCNFs) are prepared by the coaxial electrospinning of a sacrificial core solution and an emulsified shell solution containing sacrificial islands for pore generation. After a thermal treatment, a systematic study is carried out to relate the resulting pore size in pHCNFs to the sacrificial islands in the emulsified shell. As the pores are introduced in pHCNFs, their initial capacity and reversible capacity rate are proved to increase significantly to 1003 $mAhg^{-1}$ and 61.8%, respectively, compared to those (653 $mAhg^{-1}$ and 53.9%) of nonporous HCNFs. The increased pore size and expanded graphene layers are believed to facilitate lithium insertion/extraction behavior.

KEYWORDS: *porous hollow carbon nanofibers, negative electrode performance, emulsified shell solution, coaxial electrospinning*

1. INTRODUCTION

There is growing demand for advanced lithium-ion batteries (LIBs) with higher specific capacities and longer cycling performance as portable electronics increasingly employ highly powered parts for advanced performance and given that electric vehicles have emerged in the market. Commercialized electrode materials, however, have been obstacles to achieving this because their low specific capacity (i.e., graphite 372 $mAhg^{-1}$ and lithium cobalt oxide 140 $mAhg^{-1}$), promoting various types of research toward advanced LIBs.[1−4] As such, alternative electrode materials such as Si (4212 $mAhg^{-1}$), Sn (990 $mAhg^{-1}$), and S (1672 $mAhg^{-1}$) have been intensively researched because of the overwhelming theoretical capacities,[5−10] while lithium iron phosphate has been also vigorously researched because of their multifunctional performances, such as the better theoretical capacity 170 $mAhg^{-1}$, the abundance, and less toxicity compared to Co, Ni, and Mn.[11−13] Despite the superb specific capacities of these materials, their large volume change and subsequent electrical contact loss have been recognized as serious problems to be overcome.[14−19] Carbon composite electrodes have been developed,[20−25] among which the core/shell carbon nanofibers (e.g., the high-capacity anode material in the core and the carbon in the shell) are relevant to solve these problems. The carbon shell can buffer the volume change and thus maintain the electrical contact while the core materials manifest a high specific capacity.[26] Here, the carbon shell acts as a reservoir to accommodate Li-ions through intercalation, simultaneously becoming a transport medium through which Li-ions move into the core materials. Therefore, the microstructure of the carbon shell, in particular its porosity, is an important parameter to determine the movement of Li-ions and thus the anodic performance. There are, however, few

Received: September 4, 2012
Accepted: December 3, 2012
Published: December 3, 2012

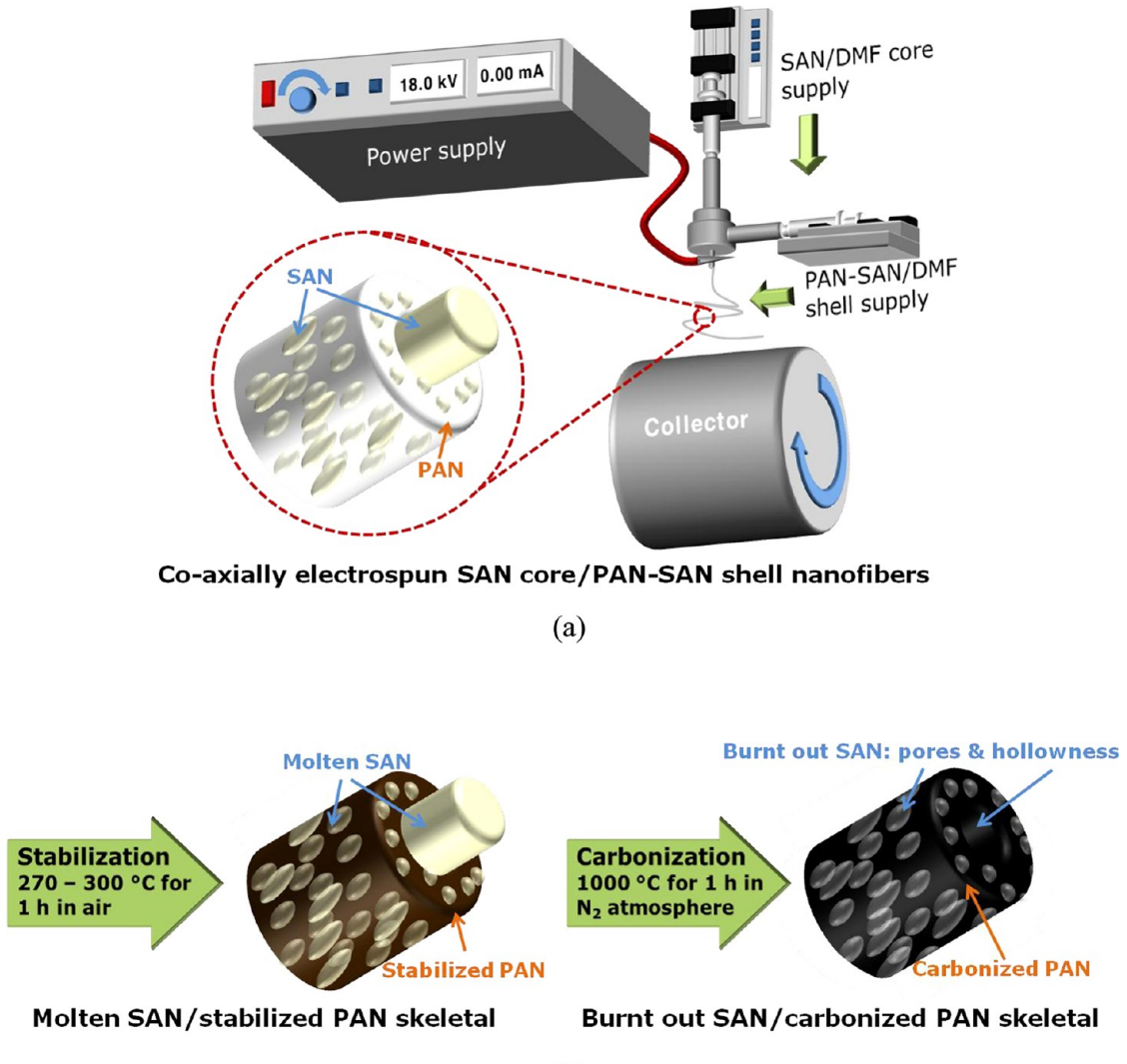

Figure 1. A schematic diagram illustrating the fabrication process of pHCNFs. (a) Coaxially electrospun SAN core/PAN-SAN shell nanofibers and (b) subsequent stabilization and carbonization of the nanofibers for manufacturing pHCNFs.

reports addressing this issue for hollow carbon nanofibers (HCNFs), which constitute the main shell component of core/shell carbon nanofibers.

It has been reported that the electrochemical performances of carbonaceous materials are improved by pores because the porosity facilitates the charge transfer at the electrode–electrolyte interface,[27] alleviates the stress induced by volume changes,[28] and supplies a viable container space.[29] Therefore, the anodic performance of solid carbon nanofibers (CNF), which are prepared by the electrospinning of poly(acrylonitrile) (PAN) solution, and a subsequent thermal treatment, are improved by these introduced pores.[27,30,31] Further improvement is achieved by compositing Si, S, or MnO_2 with porous CNFs.[29,32,33] Broadly, two methods have been used to manufacture porous CNFs: sacrificial component methods and activation methods. Ji et al. introduced the sacrificial components of poly(L-lactic acid) and SiO_2 nanoparticles into PAN solutions in an effort to synthesize advanced anode materials for LIBs.[27,34] On the other hand, Zhang and Kim introduced poly(methylmethacrylate) (PMMA)[35,36] as the sacrificial component and investigated the pore formation in detail. These polymeric sacrificial components are burnt out during the carbonization process, while the SiO_2 is dissolved by HF and subsequently extracted from the carbon matrices, leaving pores in CNFs. Note that the residue of the silicon oxide based template may result in the increase of the irreversible capacity due to the formation of the passivation layers such as lithium silicate.[37−39] The volume and width of the mesopores were reported to increase significantly according to the increased sacrificial core content,[31,36] that is, the mesopores directly originated from the sacrificial component while the micropores were formed by gas penetration during the thermal decomposition of the sacrificial component.[36] In addition, Kim et al. developed an activated method to prepare porous CNFs for synthesizing improved supercapacitors.[40] The CNFs were oxidatively stabilized and activated by a nitrogen air steam, resulting in porous CNFs. Various studies on the formation of pores in CNFs and their effects on the electrochemical properties have been carried out; however, scant research on porous hollow carbon nanofibers (pHCNF) has been performed, despite the fact that the effect of pores on the anodic properties of HCNFs is an important issue.

This work aims to develop a facile fabrication method to create pHCNFs and investigate the effect of pores on their

electrochemical performance. The coaxial electrospinning of sacrificial core and carbon shell solutions and subsequent thermal treatment method are employed to prepare pHCNFs. To form pores in the carbon shell, a styrene-*co*-acrylonitrile (SAN) solution is introduced into the PAN solution, forming SAN-island PAN-sea emulsion. This emulsion is provided as the shell solution, while another SAN solution is used as the core solution, as in previous studies.[41,42] After the thermal treatment, pores in the carbon shell are quantitatively investigated and the electrochemical performance of pHCNF is characterized while focusing on the pore effect. As the overall processing used in this study includes the emulsion preparation, the coaxial electrospinning, and thermal treatment, which are not complex, we believe that the current approach is one of the Integrative Chemistry approaches.[43]

2. EXPERIMENTAL SECTION

2.1. Materials and Fabrication. SAN (M_w = 120 000 g mol^{-1}, acrylonitrile portion = 28.5 mol %, Cheil Industries) was used as both a sacrificial core component for HNCFs and as a porous agent in the shell. PAN (M_w = 200 000 g mol^{-1}, Misui Chemical) was chosen as a carbon shell material. *N,N*-dimethylformamide (DMF, 99.5%) was used to prepare the core and shell solutions. SAN was dissolved in DMF at a concentration of 30 wt %. A mixture of PAN and SAN at a weight ratio of 3: 1 was dissolved in DMF at a concentration of 20 wt % and then emulsified. The solutions were then ultrasonicated for 5 h and additionally stirred at 80 °C for 5 h.

The coaxial electrospinning of SAN/DMF core/emulsified PAN-SAN/DMF shell solutions was carried out to manufacture SAN core/PAN-SAN shell nanofibers. Details pertaining to the electrospinning conditions can be found in the literature.[26] A subsequent thermal treatment was applied to the electrospun nanofibers for the stabilization and carbonization of the PAN shell, while the SAN in both the core and the shell was decomposed and burnt out during the thermal treatment. Details on the thermal treatment can be also found in the literature.[26] A schematic diagram illustrating the fabrication process of the pHCNFs is provided in Figure 1.

2.2. Characterizations. The emulsion of PAN and SAN used in the shell solution, in particular the size of the SAN-island particles, was quantitatively characterized using an optical microscope (BX 51, Olympus), after which the effect on the porosity of pHCNFs was investigated by means of electron microscopy. The cross-section and morphologies of the pHCNFs were investigated using a field-emission scanning electron microscope (FE-SEM) (SUPRA 55VP, Carl Zeiss). The porous microstructures of pHCNFs were investigated using a high-resolution transmission electron microscope (HR-TEM, JEM-3000F). Wide-angle X-ray diffraction (WAXD) (wavelength = 0.154 nm, New D8 Advance, Bruker) and Raman spectroscopy (wavelength:0.532 nm, NRS-3100, Jasco) were employed to characterize the carbonized structures of the pHCNFs. The porosity and surface area of pHCNFs were characterized using N_2 adsorption at 77 K using Brunauer–Emmett–Teller (BET) (Micromeritics ASAP2420). The pHCNFs were pretreated at 300 °C for 2 h to measure the surface area and porosity. X-ray photoelectron spectroscopy (XPS, VG Multilab ESCA 2000 system, Thermo Scientific) was carried out to investigate the surface functional groups.

Two-electrode 2032-type coin cells[44] were prepared to evaluate the anodic performance of the pHCNFs. The negative electrode was prepared by mixing pHCNFs (60 wt %), acetylene black (20 wt %), and poly(vinylidene floride) (20 wt %) in 1-methyl-2-pyrrolidinone. The slurry was then screen-printed onto a Cu foil and dried. For a half-cell configuration, a Li foil was used as the counter and reference electrode, while glass fibers were used as the separator. One mole of $LiPF_6$ in a mixed solution of propylene carbonate (PC) and diethyl carbonate (DEC) (volume ratio 1:1) was used as the electrolyte. The electrochemical measurements were performed at two current densities (50 and 200 mAg^{-1}) between 0.01 and 1.5 V.

3. RESULTS AND DISCUSSION

3.1. Morphologies and Microstructures of pHCNF. The shell solution (PAN-SAN/DMF) was successfully prepared as an emulsion of SAN/DMF and PAN/DMF islands-in-sea (see Figure 2a). The SAN/DMF islands, which will be directly

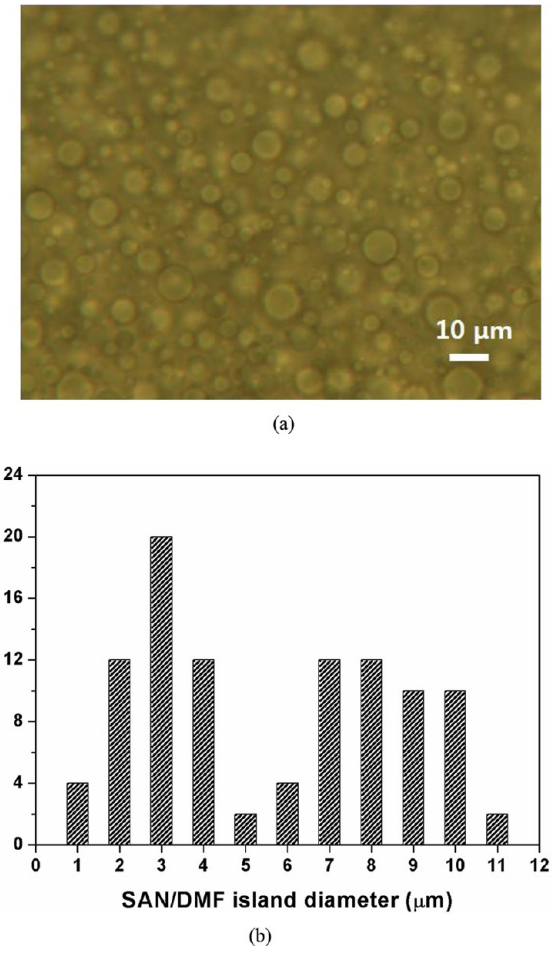

Figure 2. (a) Optical observation of PAN-SAN (3:1)/DMF emulsion and (b) the distribution of the SAN/DMF island diameter.

related to the size of pores in pHCNF later, are much smaller than PMMA/DMF islands (~100 μm) in a previous experiment by Bazilevsky et al.[45] Interestingly, the diameter of SAN/DMF islands shows a bimodal distribution with the first and second peaks at 2.90 μm (±0.98 μm) and 8.22 μm (±1.32 μm), respectively, as shown in Figure 2b. The average diameter of these islands is 5.56 μm (±2.92 μm); however, the islands are evenly distributed on both sides of the average diameter.

Microscopic images of the pHCNFs prepared by the coaxial electrospinning and subsequent thermal treatment processes

are presented in Figure 3 (a) and (b), demonstrating that pHCNFs were successfully manufactured. The cross-section

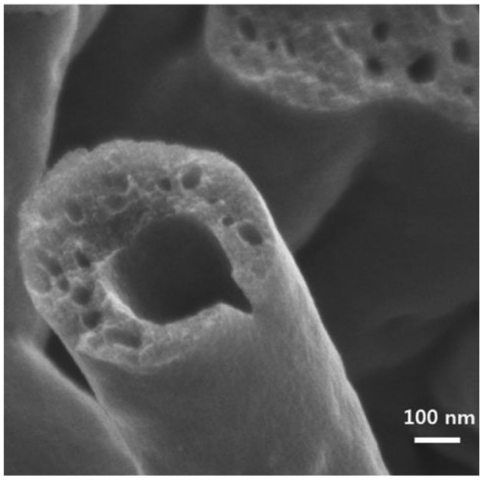

(a)

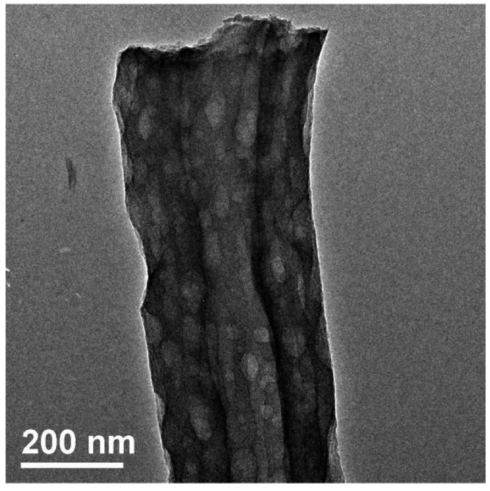

(b)

Figure 3. Microscopic images of the pHCNFs taken by (a) FE-SEM and (b) TEM.

shape of the pHCNFs is elliptical (the eccentricities of the inner and outer ellipses are 0.66 and 0.45, respectively), and the average outer diameters and wall thicknesses of the pHCNFs are 397 and 110 nm, respectively, which are smaller than those (835 and 145 nm) of nonporous HCNFs. This reduction in the diameter can be explained by the reduced viscosity of the shell solution. As shown in Table 1, the electric conductivity and the viscosity of the shell solutions are reduced due to the addition of SAN/DMF to PAN/DMF. The reduced electric conductivity increases the diameter of electrospun nanofibers because the decreased charge density of the solution bring about the less extended electrified jet during the electrospinning process. On the other hand, the reduced viscosity results in a considerable reduction of the diameters of nanofibers.[47] These two factors are competitive; however, the decreased viscosity plays a dominant role in the reduction of the outer diameter and the wall thickness in this work.

Table 1. Electrical and Rheological Properties of Shell Solution

composition (wt. %)	electric conductivity (μS/cm)	viscosity (Pa·s)
PAN 20: DMF 80[a]	139	2.28
PAN 15: SAN 5: DMF 80	113	1.51

[a]A reference shell solution from ref 42.

The microstructures of the pHCNFs were characterized by WAXD, HR-TEM, and Raman spectroscopy, as shown in Figure 4. The equatorial peaks of (002) and (101)/(100) planes at 23.7° and 43.3°, respectively, in the WAXD curve, confirm the carbonized microstructure of the pHCNFs. The (004) peak is scarcely detectable owing to the low carbonization temperature used in this study, while the (110) peak is observable around 80°. The d_{002} value (the spacing between the graphene layers) was calculated from WAXD curve as 0.375 nm, which is much larger than that of graphite (0.335 nm) or that of nonporous HCNFs (0.361 nm). The expanded d_{002} value implies that the graphene layers are displaced due to many layer-sequential mismatches occurring in the pHCNFs[42] and that there is much room for lithium ion storage. Note that the d_{002} difference between the pHCNFs and the graphite amounts to the layer expansion when the carbonaceous materials expand in volume due to intercalation during the lithiation process.[48] The value of d_{002} was also measured from the HR-TEM images shown in Figure 4, from which a similar value (0.376 nm) was obtained. In general, d_{002} is inversely proportional to the thickness of the carbon crystallite (usually measured by the number of carbon layers in the crystallite and denoted by L_c) and the crystal size (L_a), that is, as d_{002} increases, the number of the carbon layers in the carbon crystal decreases, as does the size. The crystallite thickness (L_c = 4.9 nm (±0.8)) and size (L_a = 5.00 nm (±1.10)) are, however, slightly increased compared to those of nonporous HCNFs (L_c = 4.6 (±0.8) and L_a = 4.54 nm (±0.87)).[42] As reported in earlier work,[49−51] this case is considered as a somewhat exceptional case, which cannot be explained at the moment. The inset of Figure 4b shows the typical diffraction pattern of the pHCNFs, reflecting randomly oriented polycrystallites. Such an isotropic microstructure contributes to the formation of a conductive pathway for the lithiated metals, metal oxides, metal sulfides, and sulfur and to the mechanical strength as well.[46] Figure 4c shows Raman spectrum of the pHCNFs. The Raman spectrum was deconvoluted into two Gaussian peaks. The primary peak around 1370 cm^{-1} corresponds to the breaking symmetry caused by defects or structural disorders, while the later peak around 1575 cm^{-1} is related the in-plane tangential stretch vibration mode of graphitic layer.[52] The integrated peak ratio (I_D/I_G) was calculated to be 1.60, showing that the carbonization was disturbed by the formation of a number of pores at the wall.

The precursor nanofibers of the pHCNFs consist of C, H, and N, undergoing the oxidative stabilization to form the ladder structure before carbonization. Therefore, it is expected that the pHCNFs consist of C, H, N, and O. Figure 5a shows the full range of the X-ray photoelectron spectroscopy. The peak related to C1s around 285 eV is considerable. The peaks related to N1s around 400 eV or O1s around 532 eV are much less developed, implying that the contents of O and N functional groups is negligible compared to the graphitic C−C bonds. As such, the O and N related peaks are much smaller than that of the graphitic C−C bond in the C1s spectra (see Figure 5b).

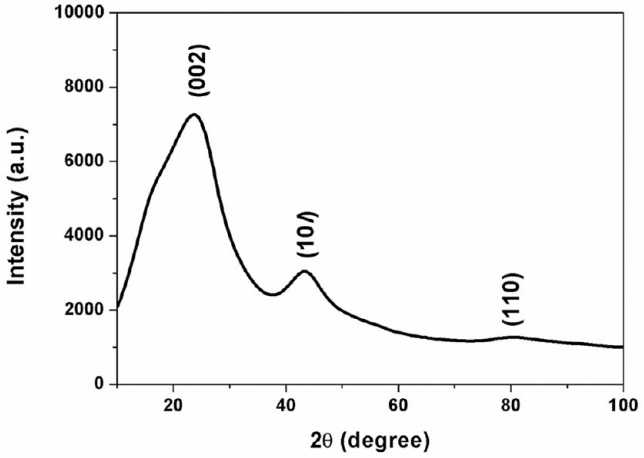

(a)

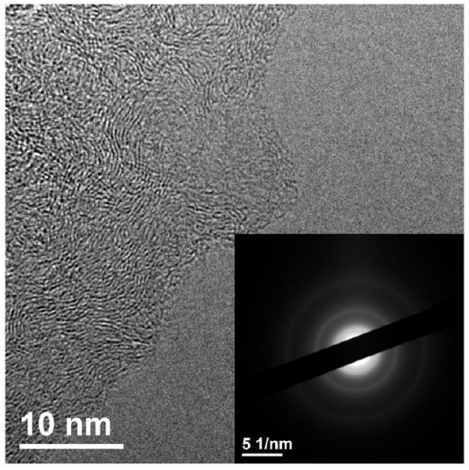

(b)

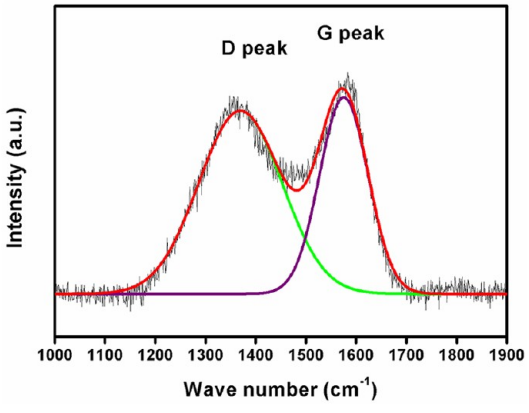

(c)

Figure 4. Microstructures of the pHCNFs. (a) WAXD curve, (b) HR-TEM image (the inset figure represents electron diffraction pattern), and (c) Raman spectrum.

The greatest deconvoluted peak around 284.6 eV is related to graphitic C−C bonds,[53] and its areal fraction is 81%. In the meantime, the miscellaneous peaks developed at higher binding energy than that of the graphitic C−C bonds represent the presence of C−O or C═N bond (at 286.3 eV), C═O bond (at 287.7 eV), and C═O−O bond (at 289.4 eV),

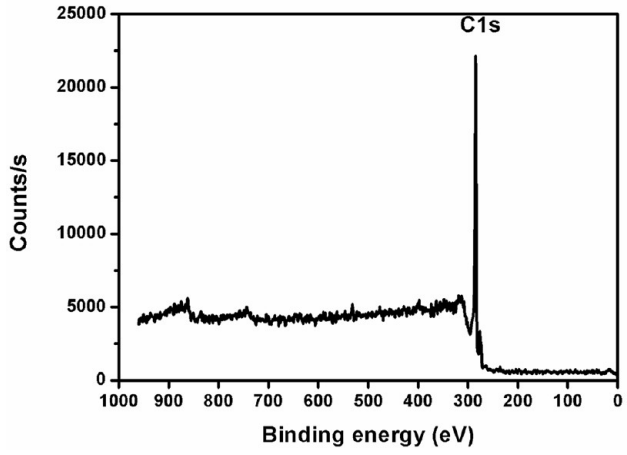

(a)

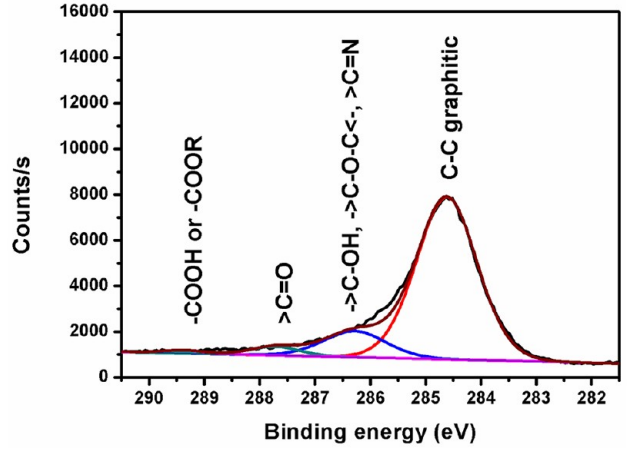

(b)

Figure 5. X-ray photoelectron spectroscopies: (a) full range spectra and (b) C1s spectra of pHCNFs.

respectively.[53] The areal fractions of these miscellaneous peaks are 14.8%, 2.9%, and 1.2%, respectively.

3.2. Pore Characterization of pHCNFs. The nitrogen adsorption isotherm of the pHCNFs is presented in Figure 6a, showing the typical behavior of nonporous carbons.[54] Furthermore, the total surface area of the pHCNFs is similar to that of the nonporous HCNFs (see Table 2). These observations are unexpected outcomes because pores are introduced into HCNFs via the burn-out of SAN in the shell during the carbonization process. The unchanged total surface area can be explained by two factors. The first is the firm interface between the SAN islands and PAN sea, which may hinder the additional evolution of micropores.[36] The second factor is the coalition of the micrcopores with neighboring micropores into mesopores or macropores, resulting in a reduced density of micropores. In fact, the pore volume and the average pore size of the pHCNFs increased by 42.6 and 41.2%, respectively, compared to those of nonporous HCNFs (see Table 2), supporting the pore coalition mechanism. Even though the surface area 13 m^2/g is small compared to the activated carbonaceous materials (thousands of m^2/g), the micro-, meso-, and macropores in the pHCNFs are much more than those of the PAN-based carbon fibers (around or less than 1 m^2/g[55,56]) in spite of their cavities. Therefore, the current surface area is still meaningful. On the other hand, the total

dx.doi.org/10.1021/am301873d | ACS Appl. Mater. Interfaces 2012, 4, 6702−6710

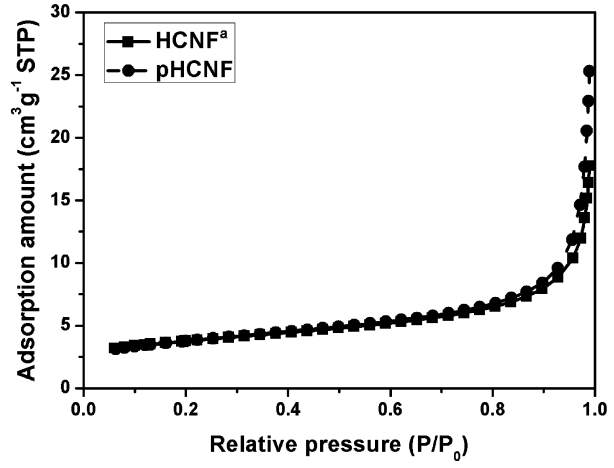

(a)

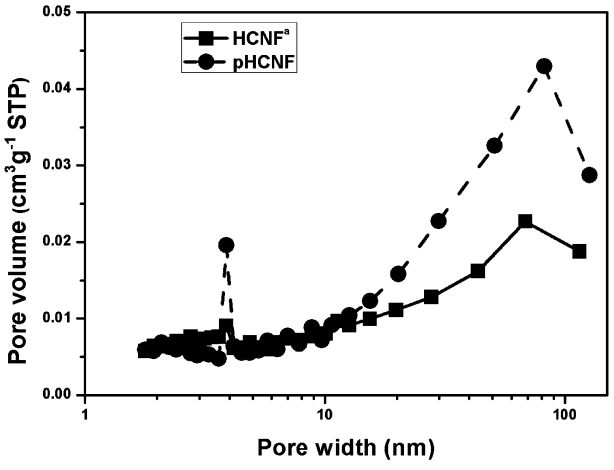

(b)

Figure 6. (a) Nitrogen adsorption isotherm of the pHCNFs and (b) their pore size distribution (BJH desorption pore volume).

Table 2. Summary of Nitrogen Adsorption Properties of pHCNFs

sample	BET SSA (m^2 g^{-1})	total pore volume (cm^3 g^{-1})	average pore size 4 V/A (nm)
Raw HCNF[a]	13	0.027	8
Porous HCNF[b]	13	0.039	12

[a]A sample prepared under the same condition in previous work.[42] [b]A sample prepared in this work.

pore volume and the average pore size of pHCNFs were significantly increased compared to raw HCNFs. The BJH desorption curves in Figure 6b also supports the increase of the meso-to-macropore volume compared to the raw HCNFs.

The stable interface and immiscibility between SAN and PAN solution[41] are considered as the origin of the small surface area. The miscible composition results in significant increase of the surface area because the mixed region can form many micro- and meso-pores during the thermal treatment. Note that Ji et. al reported very different surface areas of the porous carbon nanofibers with the same weight fraction: 235 m^2/g of PAN/PLLA (9:1)[34] and 41 m^2/g of PAN/SiO_2 (9:1).[27] As a LIB electrode material, the small surface area is more helpful due to less formation of SEI layers.

The shapes and dimensions of the pores in the pHCNFs were further examined via microscopy. FE-SEM cross-sectional image of the pHCNFs show circular pores with a density of 9.4 (±2.4) pores per cross-section (see Figure 3a), while the longitudinal TEM images shows the elliptic pore shape (see Figure 3b), implying that the actual pore is an ellipsoid, the major axis of which is parallel to the nanofiber. The elliptical pores result from the extension of SAN/DMF islands during the electrospinning process. The pore dimensions (i.e., the diameters on the minor and major axes) were measured using TEM images, as shown in Figure 7. The average diameters of

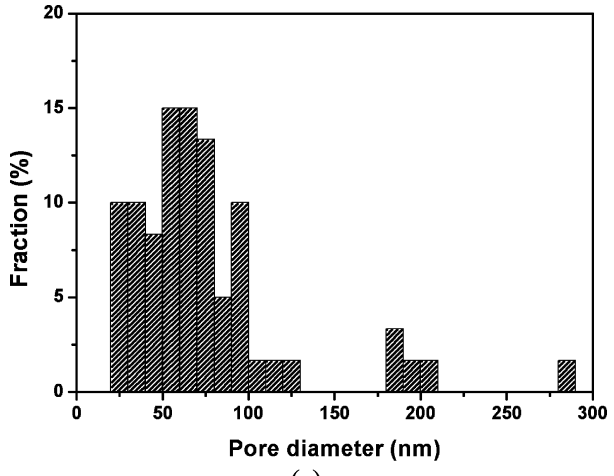

(a)

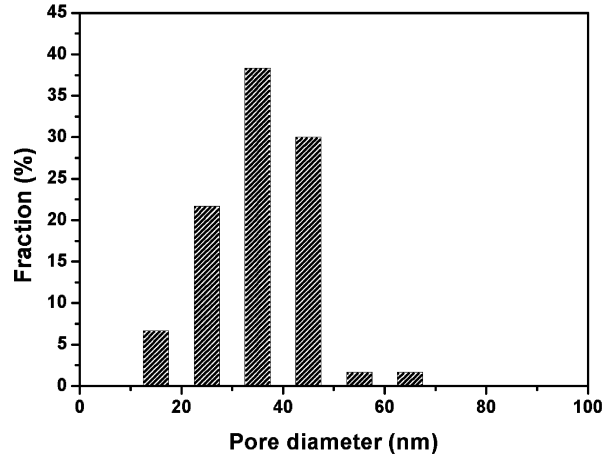

(b)

Figure 7. The size distribution ((a) major and (b) minor diameter) of pores in the pHCNFs.

the major and minor axes are 75.2 nm (±49.0 nm) and 35.1 nm (±9.0 nm), respectively. The eccentricity of the ellipse is 0.88. The large standard deviation of the pore sizes, in particular along the major axes, is caused by the bimodal distribution of SAN/DMF islands in the emulsion and the coalition of the neighboring pores. Given a SAN concentration of 20 wt %, the diameter of spherical SANs can be calculated as 1.6 and 4.8 μm by assuming a bimodal distribution of SAN/DMF islands in the emulsion (see Figure 2). The size of the pores corresponding to the SAN/DMF islands can be calculated by again assuming a

dx.doi.org/10.1021/am301873d | ACS Appl. Mater. Interfaces 2012, 4, 6702−6710

biomodal distribution of the pores. The effective diameters (i.e., the diameter of a sphere having the same volume as that of an ellipsoid) of the ellipsoids located at around 70 and 200 nm in Figure 7a are 44 and 62 nm, respectively. SAN/DMF islands appear to induce pores, the sizes of which are 25−50 times smaller than the parental islands due to anomalous thermal shrinkage,[36] suggesting that the pore size in HCNFs can be controlled by the size of SAN/DMF islands in the emulsion.

3.3. Electrochemical Performance of pHCNF. The electrochemical performance of the pHCNFs is evaluated using galvanostatic charge−discharge tests. Figure 8 shows the

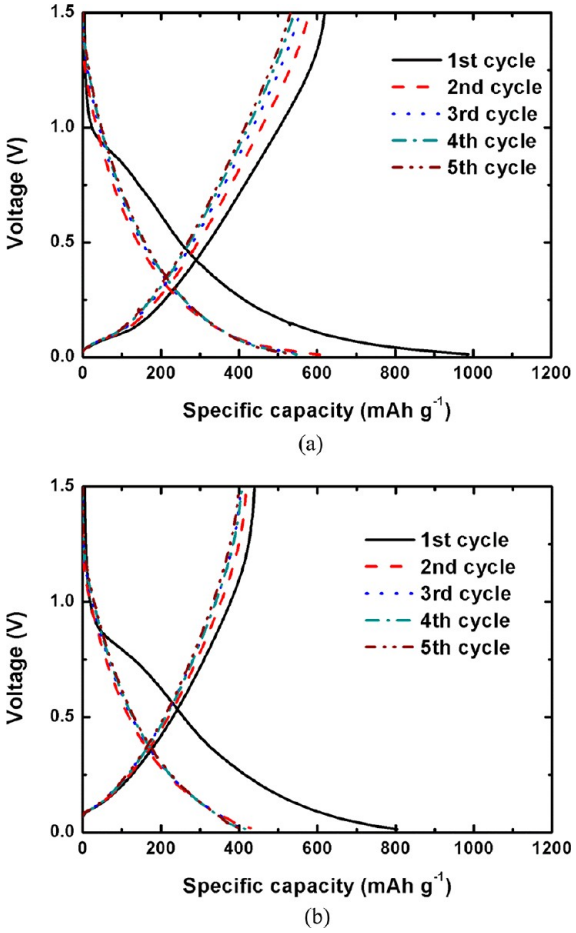

Figure 8. Voltage profiles of pHCNFs at the current density of (a) 50 and (b) 200 mAg^{-1}.

charge−discharge behavior of the pHCNFs, which is similar to that of hard carbons.[57] The two inflection points at approximately 0.8 and 0.2 V are observed on the first charge curves regardless of the current density. This behavior is compared to that of the nonporous HCNFs[42] on the differential capacity curves (see Figure 9a). The magnified curves in Figure 9b clearly show two peaks at about 0.75 and 0.85 V. These two peaks represent the formation of an irreversible passivation layer known as a solid electrolyte interface (SEI)[58] and the lithiation of the cavities,[59] respectively. For the nonporous HCNFs, SEI formation is foremost over cavity lithiation. In contrast, cavity lithiation becomes dominant for the pHCNFs due to the increased pore volume despite the decreased surface area. Note that these peaks disappear in the ensuing cycles (see Figure 8c) because of their nonrecurring nature.[59,60] On the other hand, the repetitive

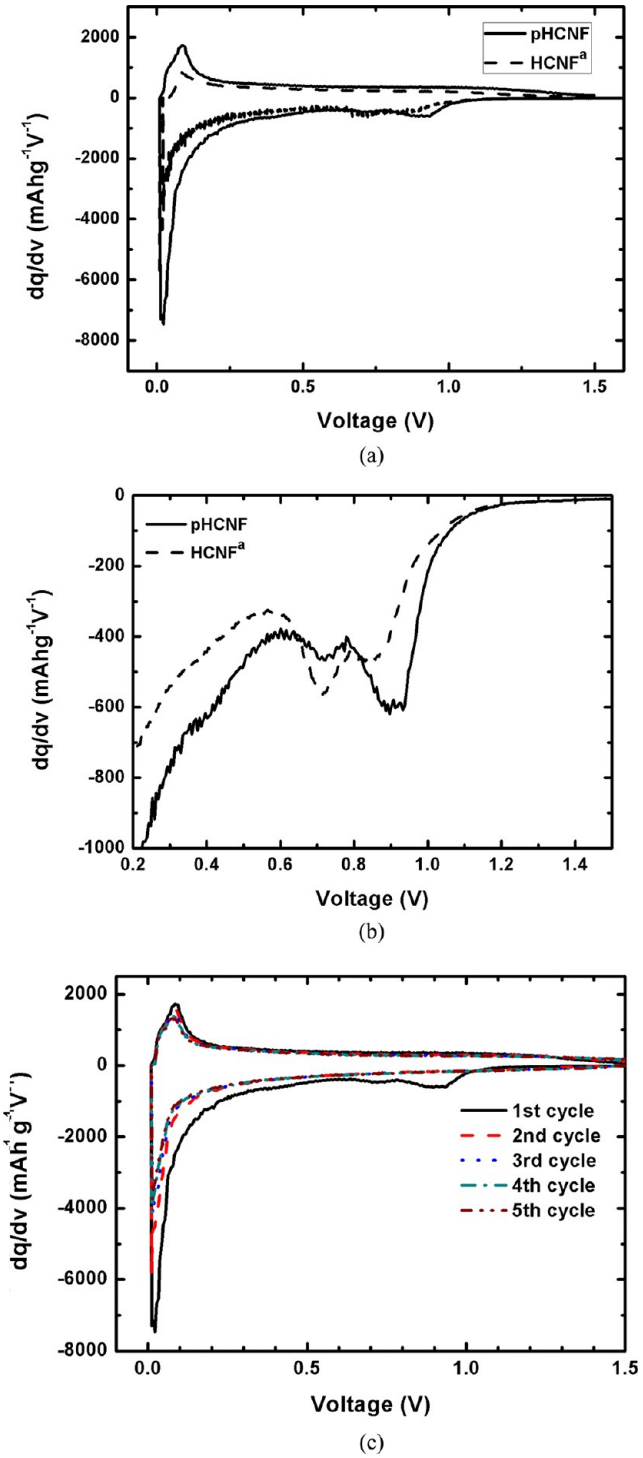

Figure 9. Differential capacity curves of the pHCNFs and nonporous HCNFs on 50 mAg^{-1}[42] during the first discharge−charge process: (a) overall curves, (b) discharge curves between 0.2 and 1.5 V, and (c) differential capacity curves of pHCNFs on 50 mAg^{-1} for the first five cycles .

peak below 0.2 V represents the formation of reversible Li_xC_6.[58] Lithiation behavior below 0.2 V is clearly repeated in subsequent cycles in the 50 mAg^{-1} case (see Figure 8a) due to the reversibility. For the 200 mAg^{-1} case, however, it considerably shortens, as shown in Figure 8b, as the reversible intercalation is disturbed by the higher current density due to the bottleneck phenomena caused by the crowded lithium ions.

dx.doi.org/10.1021/am301873d | ACS Appl. Mater. Interfaces 2012, 4, 6702−6710

The cycling performances of the pHCNFs are compared to those of the nonporous HCNFs in Figure 10. The initial

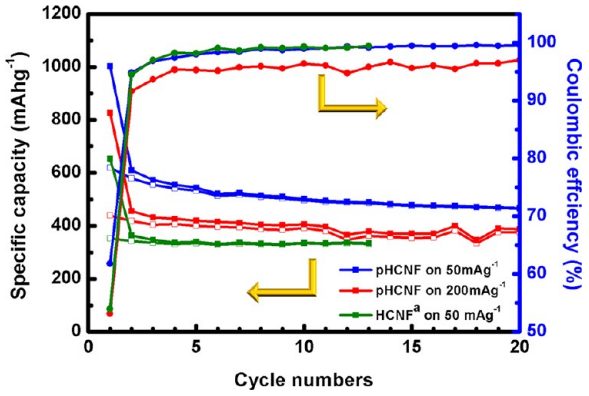

Figure 10. Comparison of cycling performances of pHCNFs to that of the nonporous HCNF.[42]

capacity and reversible capacity rate of the pHCNFs are 1003 $mAhg^{-1}$ and 61.8%, respectively, for the 50 mAg^{-1} case, which are significantly improved values compared to those (653 $mAhg^{-1}$ and 53.9%) of the nonporous HCNFs.[42] The increased pore size and expanded graphene layers are believed to facilitate lithium insertion/extraction.[34,59] As the current density increases, for example, to 200 mAg^{-1}, the initial capacity and reversible capacity rate of the pHCNFs are reduced to 827 $mAhg^{-1}$ and 53.2%, respectively. These reductions can be explained in terms of the disturbed reversible intercalation caused by the high current density (see Figure 8b). Note that the reversible capacities and Coulombic efficiencies converge within several cycles. The reversible capacities after 10 cycles are 501 and 391 $mAhg^{-1}$ for the current densities of 50 and 200 mAg^{-1}, respectively, and their Coulombic efficiencies after 10 cycles exceeds 98.99 and 96.40%, respectively. These results are not directly applied to higher rate case, for example, 300 mAg^{-1}, however, we believe that the similar trends can be observed in that case due to the carbonaceous nature of pHCNFs. It can be expected that the initial and reversible capacities of porous HCNFs (pHCNFs) may be lowered for the high current rate. This is due to the promotion of the bottleneck phenomenon of the lithium ions. The Coulombic efficiencies may be also lowered because of insufficient extraction of the lithium ions from the carbon crystallites. Interestingly, the capacity retention for the 200 mAg^{-1} case after 20 cycles is 85.1%, whereas it is 76.6% for the 50 mAg^{-1} case. Synthetically, these electrochemical characteristics demonstrate that pHCNFs are highly suitable for enhanced anodes, in particular carbon materials, which encapsulate metal or metal oxide nanoparticles. In the meantime, it can be thought that the nanofiber morphology was preserved after cycling because the reversible intercalation was maintained after the second cycle; however, systematic analyses on the morphologies and the microstructures of the nanofibers after cycling are required to conclude this consideration.

4. CONCLUSIONS

pHCNFs were successfully prepared using a coaxial electrospinning process and the emulsion of the SAN/DMF island and PAN/DMF sea as a shell solution. The relationship between the size of the SAN/DMF islands in the emulsion and the pore size in the pHCNFs was investigated by measuring the pores directly from HR-TEM images, demonstrating the possibility of manufacturing various HCNFs with controlled pore sizes and volumes. The morphological features of the pHCNFs are unique in that the pore size and volume increase while the total surface of the pores is reduced when compared to nonporous HCNFs. In addition, the spacing between the graphene layers in the pHCNFs increases due to the numerous layer-sequential mismatches which occur by the pore formation. These structural changes in HCNFs facilitate lithium-ion insertion and extraction, resulting in improved electrochemical performances. The initial capacity and reversible capacity rates are improved to 1003 $mAhg^{-1}$ and 61.8%, respectively, which are 350 $mAhg^{-1}$ and 7.9% higher than those of the nonporous HCNFs. The Coulombic efficiency shows a slight reduction, from 99.32% to 98.99%.

AUTHOR INFORMATION

Corresponding Author

*Tel.: +82 2 880 9096. Fax: +82 2 883 8197. E-mail: woongryu@snu.ac.kr.

Notes

The authors declare no competing financial interest.

ACKNOWLEDGMENTS

This research was supported by Basic Science Research Program through the National Research Foundation of Korea (NRF) funded by the Ministry of Education, Science and Technology (2010-0022633).

REFERENCES

(1) Scrosati, B. *Electrochim. Acta* **2000**, *45* (15−16), 2461−2466.
(2) Wang, C.; Yin, L.; Xiang, D.; Qi, Y. *ACS Appl. Mater. Interfaces* **2012**, *4* (3), 1636−1642.
(3) Ji, L.; Toprakci, O.; Alcoutlabi, M.; Yao, Y.; Li, Y.; Zhang, S.; Guo, B.; Lin, Z.; Zhang, X. *ACS Appl. Mater. Interfaces* **2012**, *4* (5), 2672−2679.
(4) Nithya, C.; Thirunakaran, R.; Sivashanmugam, A.; Gopukumar, S. *ACS Appl. Mater. Interfaces* **2012**, *4* (8), 4040−4046.
(5) Wang, J.; Wang, Y.; He, X.; Ren, J.; Jiang, C.; Wan, C. *J. Power Sources* **2004**, *138* (1−2), 271−273.
(6) Ng, S.-H.; Wang, J.; Wexler, D.; Konstantinov, K.; Guo, Z.-P.; Liu, H.-K. *Angew. Chem., Int. Ed.* **2006**, *45* (41), 6896−6899.
(7) Wang, G. X.; Ahn, J.-H.; Lindsay, M. J.; Sun, L.; Bradhurst, D. H.; Dou, S. X.; Liu, H. K. *J. Power Sources* **2001**, *97*−*98* (0), 211−215.
(8) Datta, M. K.; Kumta, P. N. *J. Power Sources* **2009**, *194* (2), 1043−1052.
(9) Trifonova, A.; Winter, M.; Besenhard, J. O. *J. Power Sources* **2007**, *174* (2), 800−804.
(10) Yu, X.; Xie, J.; Yang, J.; Wang, K. *J. Power Sources* **2004**, *132* (1−2), 181−186.
(11) Yamada, A.; Chung, S. C.; Hinokuma, K. *J. Electrochem. Soc.* **2001**, *148* (3), A224−A229.
(12) Gibot, P.; Casas-Cabanas, M.; Laffont, L.; Levasseur, S.; Carlach, P.; Hamelet, S.; Tarascon, J.-M.; Masquelier, C. *Nat. Mater.* **2008**, *7* (9), 741−747.
(13) Recham, N.; Armand, M.; Laffont, L.; Tarascon, J.-M. *Electrochem. Solid-State Lett.* **2009**, *12* (2), A39−A44.
(14) Chan, C. K.; Peng, H.; Liu, G.; McIlwrath, K.; Zhang, X. F.; Huggins, R. A.; Cui, Y. *Nat. Nanotechnol.* **2008**, *3* (1), 31−35.
(15) Yu, Y.; Gu, L.; Wang, C.; Dhanabalan, A.; van Aken, P. A.; Maier, J. *Angew. Chem., Int. Ed.* **2009**, *48* (35), 6485−6489.
(16) Choi, Y.-J.; Chung, Y.-D.; Baek, C.-Y.; Kim, K.-W.; Ahn, H.-J.; Ahn, J.-H. *J. Power Sources* **2008**, *184* (2), 548−552.
(17) Weydanz, W. J.; Wohlfahrt-Mehrens, M.; Huggins, R. A. *J. Power Sources* **1999**, *81*−*82* (0), 237−242.

(18) Santos-Peña, J.; Brousse, T.; Sánchez, L.; Morales, J.; Schleich, D. M. *J. Power Sources* **2001**, *97*−*98* (0), 232−234.
(19) Yuan, L.; Yuan, H.; Qiu, X.; Chen, L.; Zhu, W. *J. Power Sources* **2009**, *189* (2), 1141−1146.
(20) Liang, C.; Dudney, N. J.; Howe, J. Y. *Chem. Mater.* **2009**, *21* (19), 4724−4730.
(21) Cui, L.-F.; Yang, Y.; Hsu, C.-M.; Cui, Y. *Nano Lett.* **2009**, *9* (9), 3370−3374.
(22) Lee, K. T.; Jung, Y. S.; Oh, S. M. *J. Chem. Soc.* **2003**, *125* (19), 5652−5653.
(23) Wang, J.-Z.; Lu, L.; Choucair, M.; Stride, J. A.; Xu, X.; Liu, H.-K. *J. Power Sources* **2011**, *196* (16), 7030−7034.
(24) Wolf, H.; Pajkic, Z.; Gerdes, T.; Willert-Porada, M. *J. Power Sources* **2009**, *190* (1), 157−161.
(25) Balan, L.; Schneider, R.; Willmann, P.; Billaud, D. *J. Power Sources* **2006**, *161* (1), 587−593.
(26) Lee, B.-S.; Son, S.-B.; Park, K.-M.; Seo, J.-H.; Lee, S.-H.; Choi, I.-S.; Oh, K.-H.; Yu, W.-R. *J. Power Sources* **2012**, *206* (0), 267−273.
(27) Ji, L.; Lin, Z.; Medford, A. J.; Zhang, X. *Carbon* **2009**, *47* (14), 3346−3354.
(28) Thomassin, J.-M.; Debuigne, A.; Jérôme, C.; Detrembleur, C. *Polymer* **2010**, *51* (14), 2965−2971.
(29) Ji, L.; Rao, M.; Aloni, S.; Wang, L.; Cairns, E. J.; Zhang, Y. *Energy Environ. Sci.* **2011**, *4* (12), 5053−5059.
(30) Li, C.; Yin, X.; Chen, L.; Li, Q.; Wang, T. *J. Phys. Chem. C* **2009**, *113* (30), 13438−13442.
(31) Ji, L.; Medford, A. J.; Zhang, X. *J. Polym. Sci., Part B: Polym. Phys.* **2009**, *47* (5), 493−503.
(32) Ji, L.; Zhang, X. *Electrochem. Commun.* **2009**, *11* (4), 795−798.
(33) Ji, L.; Zhang, X. *Electrochem. Commun.* **2009**, *11* (6), 1146−1149.
(34) Ji, L.; Zhang, X. *Nanotechnology* **2009**, *20* (15), 155705.
(35) Zhang, L.; Hsieh, Y.-L. *Eur. Polym. J.* **2009**, *45* (1), 47−56.
(36) Kim, C.; Jeong, Y. I.; Ngoc, B. T. N.; Yang, K. S.; Kojima, M.; Kim, Y. A.; Endo, M.; Lee, J.-W. *Small* **2007**, *3* (1), 91−95.
(37) Brun, N.; Prabaharan, S. R. S.; Morcrette, M.; Sanchez, C.; Pécastaings, G.; Derré, A.; Soum, A.; Deleuze, H.; Birot, M.; Backov, R. *Adv. Funct. Mater.* **2009**, *19* (19), 3136−3145.
(38) Brun, N.; Prabaharan, S. R. S.; Surcin, C.; Morcrette, M.; Deleuze, H.; Birot, M.; Babot, O.; Achard, M.-F.; Backov, R. *J. Phys. Chem. C* **2011**, *116* (1), 1408−1421.
(39) Larcher, D.; Mudalige, C.; George, A. E.; Porter, V.; Gharghouri, M.; Dahn, J. R. *Solid State Ionics* **1999**, *122* (1−4), 71−83.
(40) Kim, C.; Yang, K. S. *Appl. Phys. Lett.* **2003**, *83* (6), 1216−1218.
(41) Lee, B.-S.; Park, K.-M.; Yu, W.-R.; Youk, J. *Macromol. Res.* **2012**, *20* (6), 605−613.
(42) Lee, B.-S.; Son, S.-B.; Park, K.-M.; Yu, W.-R.; Oh, K.-H.; Lee, S.-H. *J. Power Sources* **2012**, *199* (0), 53−60.
(43) Backov, R. *Soft Matter* **2006**, *2* (6), 452−464.
(44) Jung, Y. S.; Lee, S.; Ahn, D.; Dillon, A. C.; Lee, S.-H. *J. Power Sources* **2009**, *188* (1), 286−291.
(45) Bazilevsky, A. V.; Yarin, A. L.; Megaridis, C. M. *Langmuir* **2007**, *23* (5), 2311−2314.
(46) Fridrikh, S. V.; Yu, J. H.; Brenner, M. P.; Rutledge, G. C. *Phys. Rev. Lett.* **2003**, *90* (14), 144502.
(47) He, J.-H.; Wan, Y.-Q.; Yu, J.-Y. *Fibers Polym.* **2008**, *9* (2), 140−142.
(48) Krishnan, R.; Lu, T.-M.; Koratkar, N. *Nano Lett.* **2010**, *11* (2), 377−384.
(49) Vartapetyan, R. S.; Voloshchuk, A. M.; Limonov, N. A.; Romanov, Y. A. *Russ. Chem. Bull.* **1993**, *42* (3), 424−427.
(50) Semikolenov, V.; Litvak, G.; Plaksin, G. *Inorg. Mater.* **2000**, *36* (6), 591−594.
(51) Zubizarreta, L.; Arenillas, A.; Pis, J.; Pirard, J.-P.; Job, N. *J. Mater. Sci.* **2009**, *44* (24), 6583−6590.
(52) Lee, B.-S.; Yu, W.-R. *Macromol. Res.* **2010**, *18* (2), 162−169.
(53) Lee, J. S.; Kang, T. J. *Carbon* **1997**, *35* (2), 209−216.
(54) Carrott, P. J. M.; Roberts, R. A.; Sing, K. S. W. *Carbon* **1987**, *25* (1), 59−68.
(55) Pamula, E.; Rouxhet, P. G. *Carbon* **2003**, *41* (10), 1905−1915.
(56) Uchida, T.; Morikawa, Y.; Ikuta, H.; Wakihara, M.; Suzuki, K. *J. Electrochem. Soc.* **1996**, *143* (8), 2606−2610.
(57) Kaskhedikar, N. A.; Maier, J. *Adv. Mater.* **2009**, *21* (25−26), 2664−2680.
(58) Flandrois, S.; Simon, B. *Carbon* **1999**, *37* (2), 165−180.
(59) Yang, Z.-h.; Wu, H.-q. *Solid State Ionics* **2001**, *143* (2), 173−180.
(60) Mabuchi, A.; Tokumitsu, K.; Fujimoto, H.; Kasuh, T. *J. Electrochem. Soc.* **1995**, *142* (4), 1041−1046.